aerospace

MDPI

Article

Adaptive Robust Orbit Determination Technology Based on Space-Based Multi-Satellite Cooperative Observation

Ming Li, Mingying Huo *, Tianchen Wang, Yisen Ma, Xiyan Zhao and Naiming Qi

School of Astronautics, Harbin Institute of Technology, Harbin 150001, China; 22b918087@stu.hit.edu.cn (M.L.); 24b318040@stu.hit.edu.cn (T.W.); 23s018079@stu.hit.edu.cn (Y.M.); 2023110009@stu.hit.edu.cn (X.Z.); qinaimingok_hit@163.com (N.Q.)

* Correspondence: huomingying@hit.edu.cn

Abstract

To address the nonlinear orbit determination problem under multi-satellite cooperative observation, this paper proposes an orbit determination method integrating a plane-constrained observation model with adaptive robust filtering. Based on angular measurements from multiple observation nodes, a linearized observation model is constructed using spatial geometric constraints. The Maximum Correntropy Criterion is then introduced to adaptively weight each measurement component, and a hybrid kernel function is employed to suppress the effects of non-Gaussian noise and outliers. Meanwhile, an adaptive factor based on the covariance matching principle is designed to adjust the process noise intensity online, thereby improving the robustness of the Cubature Kalman Filter in state prediction and update. Simulation results under severe non-Gaussian noise show that the proposed adaptive robust cubature Kalman filter (ARCKF) reduces the position RMSE from 95.3 m for CKF to 30.8 m, corresponding to an improvement of approximately 67.7%, while increasing the computation time from 6.52 s to 7.35 s. These results indicate that the proposed method can achieve improved accuracy and robustness under uncertain measurement statistics and dynamic disturbances, making it suitable for space-based angles-only orbit determination, although further computational optimization is still required for onboard applications.

Keywords: orbit determination; robust filter; angles-only measurements; non-Gaussian noise

1. Introduction

With the explosive growth of space activities, Space Situational Awareness (SSA) plays an indispensable role in protecting space assets and monitoring non-cooperative targets [1]. Onboard orbit determination capability is a core and critical component of this function [2]. Traditional satellite orbit determination primarily relies on ground-based systems [3–5], which suffer from drawbacks such as susceptibility to communication link interruptions, poor real-time performance, and slow measurement data updates [6]. Space-based observation can effectively mitigate interference from atmospheric refraction and meteorological conditions, enabling round-the-clock continuous monitoring with higher angular measurement accuracy [7]. It has thus become a research hotspot and a crucial development direction in the field of SSA [8]. Currently, owing to the limited detection range, the tracking of highly maneuvering space targets is primarily realized through infrared and visible-light detection methods [9]. However, in contrast to radar systems, optical sensors can only provide angular measurements, such as azimuth and

Check for updates

Academic Editor: Vladimir S. Aslanov

Received: 22 April 2026
Revised: 17 May 2026
Accepted: 20 May 2026
Published: 24 May 2026

Copyright: © 2026 by the authors. Licensee MDPI, Basel, Switzerland. This article is an open access article distributed under the terms and conditions of the Creative Commons Attribution (CC BY) license.

elevation, and are unable to directly obtain multi-dimensional information, including range, velocity, and electromagnetic scattering characteristics. Moreover, optical observations are highly susceptible to illumination conditions, weather, and atmospheric disturbances, which may degrade the quality and reliability of the acquired data. Consequently, the development of fast and high-precision angles-only orbit determination methods has become an urgent requirement.

In practical space-based surveillance missions, the quality and continuity of observation data are often subject to strict limitations. Early angle-only initial orbit determination (IOD) methods proposed by Gauss [10], Laplace [11], and Gibbs [12] remain widely used today. The Gibbs problem, characterized by its purely geometric nature, can be solved directly for the Keplerian orbit of three points in space using vector analysis [13] or projective geometry [14]. In reference [15], orbit determination is achieved using five sets of azimuth measurements at unknown times without requiring any initial prior information.

When processing large-scale orbit determination data, traditional algorithms are often based on the two-body motion assumption. Under the influence of strong perturbations such as Earth's non-spherical gravity (J_2 and higher-order terms), atmospheric drag, and solar radiation pressure, the high nonlinearity of the dynamic equations can easily lead to divergence in the solution [16]. To address these issues, various filtering algorithms have been extensively studied. In reference [17], extensive research on filtering methods is conducted for both ground-based and space-based measurement models. Current mainstream filtering techniques include the extended Kalman filter (EKF) [18], improved EKF, and the unscented Kalman filter (UKF) [19]. To overcome the poor adaptability of EKF in strongly nonlinear scenarios, many scholars have proposed improved algorithms to enhance its robustness and accuracy [20–22]. Reference [23] introduces an EKF-based spaceborne angle-only orbit determination method using satellite cluster observations, constructing a novel measurement model and utilizing instantaneous observability to eliminate poor observations, thereby addressing the nonlinear transformation of measurement noise. Reference [24] employs differential algebra and a second-order Taylor expansion-based automatic domain splitting algorithm to achieve outlier detection and refined orbit determination. Reference [25] applies a sliding window batch processing (SWBP) algorithm to orbit estimation, demonstrating superior convergence speed and orbit determination accuracy compared to traditional EKF.

Although existing data-processing and estimation algorithms have made substantial progress in complex noise environments, achieving highly robust orbit determination remains challenging in large-scale satellite cluster observation scenarios and complex perturbation environments. In this paper, complex perturbation environments mainly refer to cases involving Earth's nonspherical gravity field, atmospheric drag, solar radiation pressure, unmodeled accelerations, and sensor outliers. These factors introduce strong nonlinearities and uncertain noise statistics into the dynamic and measurement models, thereby degrading the performance of conventional filtering algorithms. For example, the extended Kalman filter is sensitive to linearization errors, while the unscented Kalman filter and cubature Kalman filter still rely on sufficiently accurate noise statistical information under strongly nonlinear conditions. In addition, when unknown disturbances and measurement outliers occur, fixed process-noise and measurement-noise covariance settings can easily lead to filter-gain mismatch and may even cause short-term filter divergence. To address this, this paper proposes an orbit determination method that integrates a plane-constrained observation model with adaptive robust filtering, specifically designed for space-based optical observation conditions and complex perturbation environments. This method leverages spatial geometric constraints to transform angle-only observations into a linearized observation model with plane constraints. Furthermore, an adaptive factor

is designed based on the covariance matching principle to adjust the process noise intensity online, effectively enhancing the algorithm's robustness and orbit determination accuracy in complex environments.

The rest of this paper is organized as follows. Section 2 establishes the plane-constrained observation model for space-based multi-satellite angles-only measurements. Section 3 elaborates on the adaptive robust filtering framework and the WLS-based initial orbit determination method. Section 4 provides the simulation setup and comparative results, and Section 5 concludes the study.

2. The Observation Model

Each observation node within the constellation is capable of measuring two angles: azimuth (φ) and elevation (θ). The azimuth angle is defined as the angle between the projection of the target direction onto the local horizontal plane and the reference direction, representing the target position in the horizontal direction. The elevation angle is defined as the angle between the target direction and the local horizontal plane, representing the target position relative to the observer in the vertical direction. These measurements allow for the construction of a line-of-sight vector (LOS) within the node's body-fixed coordinate system, which points from the observation node toward the target.

$$\boldsymbol{L} = \begin{bmatrix} \cos\theta \sin\varphi \\ \cos\theta \cos\varphi \\ \sin\theta \end{bmatrix} \tag{1}$$

Transform the line-of-sight vector from the body frame to the LVLH frame:

$$\begin{aligned} \boldsymbol{L}_{LVLH} &= R(\theta_x)R(\theta_y)R(\theta_z)\boldsymbol{L} \\ &= \begin{bmatrix} 1 & 0 & 0 \\ 0 & \cos\theta_x & -\sin\theta_x \\ 0 & \sin\theta_x & \cos\theta_x \end{bmatrix} \begin{bmatrix} \cos\theta_y & 0 & \sin\theta_y \\ 0 & 1 & 0 \\ -\sin\theta_y & 0 & \cos\theta_y \end{bmatrix} \begin{bmatrix} \cos\theta_z & -\sin\theta_z & 0 \\ \sin\theta_z & \cos\theta_z & 0 \\ 0 & 0 & 1 \end{bmatrix} \boldsymbol{L} \end{aligned} \tag{2}$$

where θ_x, θ_y, and θ_z are the roll, pitch, and yaw angles of the observation node. The LOS is rotated from the observation node's body frame to the ECI frame.

$$\boldsymbol{L}_{ECI} = \begin{bmatrix} \cos\phi & -\sin\phi & 0 \\ \sin\phi & \cos\phi & 0 \\ 0 & 0 & 1 \end{bmatrix} \begin{bmatrix} 1 & 0 & 0 \\ 0 & \cos i & -\sin i \\ 0 & \sin i & \cos i \end{bmatrix} \begin{bmatrix} \cos\Omega & -\sin\Omega & 0 \\ \sin\Omega & \cos\Omega & 0 \\ 0 & 0 & 1 \end{bmatrix} \boldsymbol{L}_{LVLH} \tag{3}$$

where ϕ is the sum of the true anomaly and the argument of perigee, i is the orbital inclination, and Ω is the right ascension of the ascending node. Subsequent vectors are, by default, expressed in the ECI frame.

The target's state vector is defined as:

$$\boldsymbol{X}_{Tar} = [\boldsymbol{R}_{Tar}\ \boldsymbol{V}_{Tar}]^T = [x_{Tar}, y_{Tar}, z_{Tar}, \dot{x}_{Tar}, \dot{y}_{Tar}, \dot{z}_{Tar}]^T \tag{4}$$

The state vector of the Nth observation node is defined as:

$$\boldsymbol{X}_{ObsN} = [\boldsymbol{R}_{ObsN}\ \boldsymbol{V}_{ObsN}]^T = [x_{ObsN}\ y_{ObsN}\ z_{ObsN}\ \dot{x}_{ObsN}\ \dot{y}_{ObsN}\ \dot{z}_{ObsN}]^T \tag{5}$$

The observation of a single target by multiple nodes yields a set of line-of-sight vectors. The LOS from the Nth observation node to the target can be represented as:

$$\boldsymbol{L}_N = \begin{bmatrix} x_{ObsN\to Tar} & y_{ObsN\to Tar} & z_{ObsN\to Tar} \end{bmatrix}^T \tag{6}$$

To fully exploit the informational advantage of multi-satellite collaborative observation, this work is based on the geometric principle that a line in three-dimensional space is uniquely determined by the intersection of two non-parallel planes. By defining two orthogonal planes, each containing the Nth observation node and the target, using the satellite's known position and the measured LOS, the angular measurements are incorporated into the plane equations, thus converting them into geometric constraints on the target's inertial position.

In the ECI frame, the direction vector from the origin to the observation node is given by:

$$\boldsymbol{R}_{O\to ObsN} = \frac{\boldsymbol{R}_{ObsN}}{\|\boldsymbol{R}_{ObsN}\|} = \begin{bmatrix} x_{O\to ObsN} & y_{O\to ObsN} & z_{O\to ObsN} \end{bmatrix}^T \tag{7}$$

The normal vector of the first plane is defined as the cross product of the line-of-sight vector in Equation (6) and the direction vector in Equation (7):

$$\boldsymbol{n}_N = \boldsymbol{L}_N \times \boldsymbol{R}_{O\to ObsN} = \begin{bmatrix} x_{LRN,1} & y_{LRN,1} & z_{LRN,1} \end{bmatrix}^T \tag{8}$$

If $\|\boldsymbol{n}_N\| \leq 10^{-6}$, it indicates poor observation geometry, and this measurement vector should be discarded. Geometrically, this implies that the LOS vector is nearly parallel to the radial direction vector of the observation satellite in the ECI frame, causing the cross product used to construct the plane normal vector to approach zero. As a result, the corresponding plane constraint becomes ill-conditioned, and such observations are discarded to prevent degradation of the estimation accuracy. Using the known position of the observation node, the equation of the plane is given by:

$$x_{LRN,1}(x_{Tar} - x_{ObsN}) + y_{LRN,1}(y_{Tar} - y_{ObsN}) + z_{LRN,1}(z_{Tar} - z_{ObsN}) = 0 \tag{9}$$

Similarly, the second plane is defined in an analogous manner to the first. Its normal vector is calculated as the cross product of the first plane's normal vector (from Equation (8)) and the line-of-sight vector (from Equation (6)), ensuring orthogonality between the two planes. Consequently, incorporating the observation node's position yields the equation for the second plane as:

$$\boldsymbol{m}_N = \boldsymbol{n}_N \times \boldsymbol{L}_N = \begin{bmatrix} x_{nLN,2} & y_{nLN,2} & z_{nLN,2} \end{bmatrix}^T \tag{10}$$

$$x_{nLN,2}(x_{Tar} - x_{ObsN}) + y_{nLN,2}(y_{Tar} - y_{ObsN}) + z_{nLN,2}(z_{Tar} - z_{ObsN}) = 0 \tag{11}$$

By combining the plane equations given in Equations (9) and (11), we obtain:

$$\begin{bmatrix} x_{LRN,1} & y_{LRN,1} \\ x_{nLN,2} & y_{nLN,2} \end{bmatrix} \begin{bmatrix} \frac{x_{Tar}-x_{ObsN}}{z_{Tar}-z_{ObsN}} \\ \frac{y_{Tar}-y_{ObsN}}{z_{Tar}-z_{ObsN}} \end{bmatrix} + \begin{bmatrix} z_{LRN,1} \\ z_{nLN,2} \end{bmatrix} = 0 \tag{12}$$

By separating the measured quantities from the computed quantities in the equation, the final computational formula can be written as:

$$\begin{bmatrix} x_{ObsN,1} & y_{ObsN,1} \\ x_{ObsN,2} & y_{ObsN,2} \end{bmatrix}^{-1} \begin{bmatrix} z_{ObsN,1} \\ z_{ObsN,2} \end{bmatrix} = \begin{bmatrix} \frac{x_{Tar}-x_{ObsN}}{z_{ObsN}-z_{Tar}} \\ \frac{y_{Tar}-y_{ObsN}}{z_{ObsN}-z_{Tar}} \end{bmatrix} \tag{13}$$

where the matrix product on the left-hand side of the equation depends solely on the measurements from the observation node, whereas the term $(x_{Tar}, y_{Tar}, z_{Tar})$ on the right-hand side represents the target's orbital information to be estimated. This observation model is suitable for subsequent filter computations.

In summary, this chapter establishes a measurement model applicable to space-based multi-satellite cooperative observation, in which multi-satellite angles-only observation data are equivalently represented as two sets of orthogonal geometric constraints. This modeling approach transforms the observation vectors into a unified constraint formulation, allowing them to be directly incorporated into the constraint equations. Therefore, the proposed model effectively reduces the complexity of multi-source observation fusion and lays a foundation for the subsequent design of the adaptive robust orbit determination algorithm.

3. Adaptive Robust Filter Framework

It is assumed that the target's dynamics follow the Keplerian two-body motion model, whose expression is given by:

$$\dot{\hat{\boldsymbol{X}}}_{Tar} = \hat{f}(\hat{\boldsymbol{X}}_{Tar}) = \begin{bmatrix} \hat{\boldsymbol{V}}_{Tar} \\ -\frac{\mu \boldsymbol{R}_{Tar}}{|\boldsymbol{R}_{Tar}|^3} \end{bmatrix} \tag{14}$$

However, in actual orbital dynamics, perturbations and other factors introduce a process noise, denoted as ω. Consequently, the complete dynamics equation for the target is given by:

$$\dot{\boldsymbol{X}}_{\mathrm{Tar}} = f(\boldsymbol{X}_{\mathrm{Tar}}) + \omega \tag{15}$$

3.1. Maximum Correntropy Criterion

The traditional least squares criterion is sensitive to outliers. To mitigate the impact of measurement anomalies on filtering performance, the Maximum Correntropy Criterion (MCC) is introduced to assign weights to individual measurement components. For random variables x and y, the correntropy is defined as:

$$V(x, y) = E[\varphi(x, y)] \tag{16}$$

where φ is the kernel function, which is typically chosen to be the Gaussian kernel, defined as:

$$\varphi(x, y) = G_\delta(e) = exp\left(-\frac{e^2}{2\delta^2}\right) \tag{17}$$

where $e = x - y$ and δ represent the bandwidth of the Gaussian kernel. However, in systems with multidimensional noise, the Gaussian kernel is prone to matrix singularity issues when the error increases, whereas the Cauchy kernel can avoid this problem. Its functional form is given by:

$$\varphi(e) = \frac{1}{1 + e^2/\delta} \tag{18}$$

Given the relatively low accuracy of the Cauchy kernel function, a hybrid kernel function is constructed to balance both accuracy and robustness.

$$K(e) = \alpha \cdot G_\delta(e) + (1 - \alpha) \cdot \varphi(e) \tag{19}$$

where $\alpha \in [0.5, 0.7]$ represents the empirical interval. The Gaussian kernel provides high estimation accuracy under nominal noise conditions, while the Cauchy kernel offers stronger robustness against large errors and outliers. A larger α emphasizes the Gaussian term, whereas a smaller α increases the contribution of the Cauchy term. Within the interval [0.5, 0.7], the two weights vary smoothly, and the Cauchy component remains sufficiently active to maintain filtering robustness. In this study, α is set to 0.6 to balance the es-

timation accuracy of the Gaussian kernel and the outlier-suppression capability of the Cauchy kernel.

In practical measurements, directly calculating the theoretical correntropy is challenging due to limited sampling data from sensors and the inability to obtain the joint distribution of the state variables and noise. Therefore, the non-parametric estimation method in [26] is adopted to approximate the theoretical expectation by the empirical mean with a kernel function satisfying Mercer's theorem. Its expression is given as follows:

$$\hat{V}(X,Y) = \frac{1}{N}\sum_{i=1}^{N} K(e_i) \tag{20}$$

3.2. Adaptive Robust Filter

To effectively integrate MCC with the Cubature Kalman Filter (CKF) for handling the nonlinearities in orbital dynamics, a nonlinear regression model is first constructed. In the following derivation, the subscript t is used for the target state and its prior information, while the subscript k is used for the measurement quantities. The augmented terms involving both the state prior and the measurement are denoted by the combined subscript (t,k). The joint nonlinear model combining the orbital state and the observed measurements is expressed as:

$$\begin{bmatrix} \boldsymbol{x}_{t|t-1} \\ \boldsymbol{z}_k \end{bmatrix} = \begin{bmatrix} \boldsymbol{x}_t \\ \boldsymbol{h}_k(\boldsymbol{x}_t) \end{bmatrix} + \begin{bmatrix} \boldsymbol{\omega}_{x,t|t-1} \\ \boldsymbol{\nu}_k \end{bmatrix} \tag{21}$$

where $\hat{\mathbf{x}}_{t|t-1}$ is the prior estimate of the state at time t, $\omega_{x,t|t-1}$ is the prior estimation error with a covariance matrix $P_{t|t-1}$, and $\boldsymbol{\xi}_{t,k} = \left[\boldsymbol{\omega}_{x,t|t-1}, \boldsymbol{\nu}_k\right]$ is the augmented noise, whose covariance matrix is given by:

$$E\left[\boldsymbol{\xi}_{t,k}\boldsymbol{\xi}_{t,k}^T\right] = \begin{bmatrix} P_{t|t-1} & 0 \\ 0 & R_k \end{bmatrix} = D_{t,k}D_{t,k}^T \tag{22}$$

$$D_{t,k} = \begin{bmatrix} D_{p,t|t-1} & 0 \\ 0 & D_{r,k} \end{bmatrix} \tag{23}$$

where $D_{p,t|t-1}$ and $D_{r,k}$ are the Cholesky decomposition factors of $P_{t|t-1}$ and R_k, respectively, and R_k is the measurement noise covariance matrix. In the augmented noise vector $\boldsymbol{\xi}_k$, the numerical scales of the state prediction error and the measurement noise error may differ significantly. Directly combining them could cause the filter to become overly sensitive to errors with larger magnitudes. Multiplying both sides of the joint model by D_k^{-1} yields the model:

$$\boldsymbol{G}_{t,k} = b_{t,k}(\boldsymbol{x}_t) + \boldsymbol{e}_k \tag{24}$$

where $\boldsymbol{G}_{t,k} = D_{t,k}^{-1}\left[\boldsymbol{x}_{t\,|\,t-1}, \boldsymbol{z}_k\right]^T$, $\boldsymbol{b}_{t,k}(\boldsymbol{x}_t) = D_{t,k}^{-1}\left[\boldsymbol{x}_t, \boldsymbol{h}_k(\boldsymbol{x}_t)\right]^T$, and $\boldsymbol{e}_{t,k} = D_{t,k}^{-1}\left[\boldsymbol{\omega}_{x,t\,|\,t-1} \quad \boldsymbol{\nu}_k\right]^T$. The covariance of the new noise $\widetilde{\boldsymbol{\xi}}_k = D_k^{-1}\boldsymbol{\xi}_k$ is given by:

$$E\left[\widetilde{\boldsymbol{\xi}}_{t,k}\widetilde{\boldsymbol{\xi}}_{t,k}^T\right] = D_k^{-1}E\left[\boldsymbol{\xi}_{t,k}\boldsymbol{\xi}_{t,k}^T\right]\left(D_k^{-1}\right)^T = D_k^{-1}\begin{bmatrix} P_{k|k-1} & 0 \\ 0 & R_k \end{bmatrix}\left(D_k^{-1}\right)^T = I \tag{25}$$

thus achieving scale unification between the state prediction error and the measurement noise error. A cost function is formulated based on MCC with the optimization objective of maximizing the correlation between observations and estimates:

$$J(\boldsymbol{x}_t) = \sum_{i=1}^{M} K(\boldsymbol{G}_{t,k,i} - b_{t,k,i}(\boldsymbol{x}_t)) \tag{26}$$

where M represents the dimensionality of the augmented residual vector $\boldsymbol{e}_{t,k}$. Differentiating the cost function with respect to $\boldsymbol{x}_t$ yields the optimal estimation condition:

$$\left(\frac{\partial b_{t,k}(\boldsymbol{x}_t)}{\partial \boldsymbol{x}_t}\right)^T W_{t,k}(\boldsymbol{G}_{t,k} - b_{t,k}(\boldsymbol{x}_t)) = 0 \tag{27}$$

where $W_{t,k} = \mathrm{diag}(K(e_{t,k,1}), K(e_{t,k,2}), \ldots, K(e_{t,k,M}))$ is the hybrid-kernel correntropy weighting matrix. Since $W_{t,k}$ is constructed from the augmented residual vector, it contains both state-prior-related and measurement-related weights. Therefore, only the measurement-related sub-block $W_{r,k}$ is used to modify the measurement covariance. Specifically, if the state dimension is n and the measurement dimension is m, $W_{r,k}$ is obtained by extracting the last m diagonal elements of $W_{t,k}$. The modified measurement covariance is then given by:

$$\widetilde{R}_k = D_{r,k} W_{r,k}^{-1} D_{r,k}^T \tag{28}$$

3.3. The Adaptive Factor

Given the difficulty in accurately characterizing the system process noise, which is predominantly non-Gaussian, this paper introduces an adaptive factor to enhance the robustness of the filtering algorithm. The adaptive factor is designed based on covariance matching, which ensures consistency between the theoretical innovation covariance and the covariance estimated from the innovation sequence. By dynamically adjusting the filter gain using real-time innovation information, this approach compensates for estimation bias caused by unknown process noise, suppresses filter divergence, and balances the weighting between the prior state estimate and the observation information. Consequently, it improves the stability and accuracy of orbit state estimation. Based on the above definitions, the prior covariance matrix $P_{k|k-1}$ is modified, and the correction method can be expressed as:

$$P_{k|k-1}^{\alpha} = \lambda_k P_{k|k-1} \tag{29}$$

where $P_{k|k-1}^{\alpha}$ is the modified prior covariance matrix, and λ_k is the adaptive factor. According to [25], the covariance matching-based adaptive fading factor λ_k satisfies:

$$\lambda_k = \frac{\mathrm{trace}(H_k \overline{P}_{k|k-1} H_k^T)}{\mathrm{trace}(H_k P_{k|k-1} H_k^T)} = \frac{\mathrm{trace}(\overline{P}_{zz,k|k-1} - R_k)}{\mathrm{trace}(P_{zz,k|k-1} - R_k)} \tag{30}$$

where H_k is the system measurement matrix, $\mathbf{P}_{zz,k|k-1}$ represents the theoretical innovation covariance, $\overline{P}_{k|k-1}$ denotes the estimated prior covariance, and $\overline{P}_{zz,k|k-1}$ stands for the estimated innovation covariance.

The mismatch between $P_{zz,k|k-1}$ and $\overline{P}_{zz,k|k-1}$ mainly arises from an inaccurate specification of the process noise covariance $\boldsymbol{Q}_k$ [27]. Therefore, adaptive adjustment of $\boldsymbol{Q}_k$ is required. These disturbances are uniformly modeled as a continuous-time white noise acceleration process, with its power spectral density denoted as q. For the six-dimensional position–velocity state with sampling interval Δt, discretizing the white-noise acceleration model yields the following classical discrete process noise covariance matrix:

$$Q_0 = q \begin{bmatrix} \frac{\Delta t^3}{3} \boldsymbol{I}_3 & \frac{\Delta t^2}{2} \boldsymbol{I}_3 \\ \frac{\Delta t^2}{2} \boldsymbol{I}_3 & \Delta t \boldsymbol{I}_3 \end{bmatrix} \tag{31}$$

To achieve this adaptive adjustment, the following parameterized scaling strategy is employed:

$$\boldsymbol{Q}_k = \lambda_k \boldsymbol{Q}_{k-1} \tag{32}$$

This method preserves the original structure of the process noise while only adjusting its overall magnitude. This makes the adaptive adjustment more physically consistent, as it does not disrupt the correlations among different states.

3.4. Cubature Point Generation and State Update

For an n-dimensional state vector, $2n$ cubature points are generated as follows:

$$\boldsymbol{X}_{i,k-1|k-1} = \hat{\boldsymbol{X}}_{k-1|k-1} + \sqrt{n} \cdot \boldsymbol{S}_{k-1|k-1} \cdot e_i, i = 1, 2, \ldots, 2n \tag{33}$$

where $\boldsymbol{S}_{k-1|k-1}$ is the Cholesky factor of the state covariance matrix $\boldsymbol{P}$,$\boldsymbol{P}_{k-1} = \boldsymbol{S}_{k-1|k-1}\boldsymbol{S}_{k-1|k-1}^T$, and e_i is a unit vector. The cubature points are propagated through the dynamic equation, yielding the transformed points:

$$\boldsymbol{X}_{i,k|k-1} = f(\boldsymbol{X}_{i,k-1|k-1}) + \boldsymbol{w}_{i,k} \tag{34}$$

The prior state and covariance are estimated as follows:

$$\hat{\boldsymbol{x}}_{k|k-1} = \frac{1}{2n}\sum_{i=1}^{2n} \boldsymbol{X}_{i,k|k-1} \tag{35}$$

$$\boldsymbol{P}_{k|k-1} = \frac{1}{2n}\sum_{i=1}^{2n}\left(\boldsymbol{X}_{i,k|k-1} - \boldsymbol{x}_{i,k|k-1}\right)\left(\boldsymbol{X}_{i,k\,|\,k-1} - \boldsymbol{x}_{i,k\,|\,k-1}\right)^T + \widetilde{\boldsymbol{Q}}_{k-1} \tag{36}$$

where $\widetilde{\boldsymbol{Q}}_{k-1}$ represents the adaptively modified process noise covariance matrix. The cubature points are substituted into the observation model to obtain the predicted observation cubature points:

$$\boldsymbol{Z}_{i,k|k-1} = h(\boldsymbol{X}_{i,k|k-1}) + \boldsymbol{v}_{i,k} \tag{37}$$

The predicted observation mean and covariance are estimated as follows:

$$\hat{\boldsymbol{z}}_{k|k-1} = \frac{1}{2n}\sum_{i=1}^{2n} \boldsymbol{Z}_{i,k|k-1} \tag{38}$$

$$\boldsymbol{P}_{zz,k|k-1} = \frac{1}{2n}\sum_{i=1}^{2n}\left(\boldsymbol{Z}_{i,k|k-1} - \hat{\boldsymbol{z}}_{k|k-1}\right)\left(\boldsymbol{Z}_{i,k\,|\,k-1} - \hat{\boldsymbol{z}}_{k\,|\,k-1}\right)^T + \widetilde{\boldsymbol{R}}_k \tag{39}$$

where $\widetilde{\mathbf{R}}_k$ is the measurement noise covariance matrix modified based on the Gaussian–Cauchy hybrid kernel function, which effectively mitigates the impact of non-Gaussian noise. The cross-covariance is as follows:

$$\boldsymbol{P}_{xz,k|k-1} = \frac{1}{2n}\sum_{i=1}^{2n} \boldsymbol{X}_{i,k|k-1}\boldsymbol{Z}_{i,k|k-1}^T - \hat{\boldsymbol{X}}_{k|k-1}\hat{\boldsymbol{Z}}_{k|k-1}^T \tag{40}$$

The Kalman gain is as follows:

$$\boldsymbol{K}_k = \boldsymbol{P}_{xz,k|k-1}\boldsymbol{P}_{zz,k|k-1}^{-1} \tag{41}$$

The posterior state and covariance are updated as follows:

$$\hat{\boldsymbol{x}}_k = \hat{\boldsymbol{x}}_{k|k-1} + \boldsymbol{K}_k\boldsymbol{\tau}_k \tag{42}$$

$$\boldsymbol{P}_{k|k} = \boldsymbol{P}_{k|k-1} - \boldsymbol{K}_k\boldsymbol{P}_{zz,k|k-1}\boldsymbol{K}_k^T \tag{43}$$

where $\boldsymbol{\tau}_k = z_k - \hat{\boldsymbol{z}}_{k|k-1}$ is the innovation residual.

3.5. Initial Orbit Determination

The primary objective of initial orbit determination is to provide convergent and feasible initial values for the filtering algorithm, rather than pursuing extremely high precision. A relatively optimal initial value can be quickly obtained using the least squares method. The line-of-sight vector from the Nth observation node to the target can be expressed by the following linear equation:

$$\boldsymbol{r}_0 = \boldsymbol{R}_{ObsN}(t_1) + k_{N,1} \cdot \boldsymbol{L}_N(t_1) \tag{44}$$

where $k_{N,1}$ represents the range from the Nth node to the target at time t_1. By utilizing multiple observation nodes, an overdetermined system of equations can be constructed. A weighting coefficient ω_N is introduced to quantify the reliability of the observation data from different nodes.

$$\omega_N = \frac{\dfrac{1}{\sigma_N^2 + 1}}{\sum\limits_{j=1} \dfrac{1}{\sigma_j^2 + 1}} \tag{45}$$

where σ denotes the measurement noise variance. For the N observation nodes, the weighted least squares cost function is formulated as follows:

$$J = \sum_{i=1}^{N} \omega_N \cdot \left\| (r_0 - R_{Obsi}(t_1)) \times \boldsymbol{L}_i(t_1) \right\|^2 \tag{46}$$

Minimizing J achieves optimal geometric intersection. Substituting the linear equation into the cost function, taking the partial derivative with respect to r_0, and setting the derivative to zero yields the following system of linear equations:

$$A \cdot r_0 = b \tag{47}$$

where $A = \sum\limits_{N=1} \boldsymbol{\omega}_N \cdot \left[\boldsymbol{I} - \boldsymbol{L}_N(t_1)\boldsymbol{L}_N^T(t_1)\right]$, and $b = \sum\limits_{N=1} \boldsymbol{\omega}_N \cdot \left[\boldsymbol{I} - \boldsymbol{L}_N(t_1)\boldsymbol{L}_N^T(t_1)\right] \cdot \boldsymbol{R}_{ObsN}(t_1)$.

The velocity $\boldsymbol{v}_0$ can be approximately estimated from two consecutive measurements taken over a short time interval.

$$\boldsymbol{v}_0 = \frac{\boldsymbol{r}_1 - \boldsymbol{r}_0}{t_1 - t_0} \tag{48}$$

In summary, this chapter develops an adaptive robust filtering framework and a weighted least-squares initial orbit determination method. By introducing an adaptive adjustment mechanism, the proposed algorithm can dynamically modify the filtering weights when the statistical characteristics of the observation noise are inaccurate, thereby reducing the influence of abnormal observations on the estimation results. Therefore, the proposed method exhibits favorable robustness in complex space environments characterized by uncertain noise and anomalous measurements.

4. Simulation

To validate the effectiveness of the proposed algorithm, this paper conducts simulation experiments focusing on the spacecraft orbit determination problem. The experiment employs four observer satellites to perform continuous measurements on a single target. The same target and observer orbital configuration is used in all three scenarios, and the observer satellites are denoted as Observer_1–Observer_4. The observation scenario is illustrated in Figure 1, where L_1–L_4 represent the line-of-sight observation vectors from the observer satellites to the target.

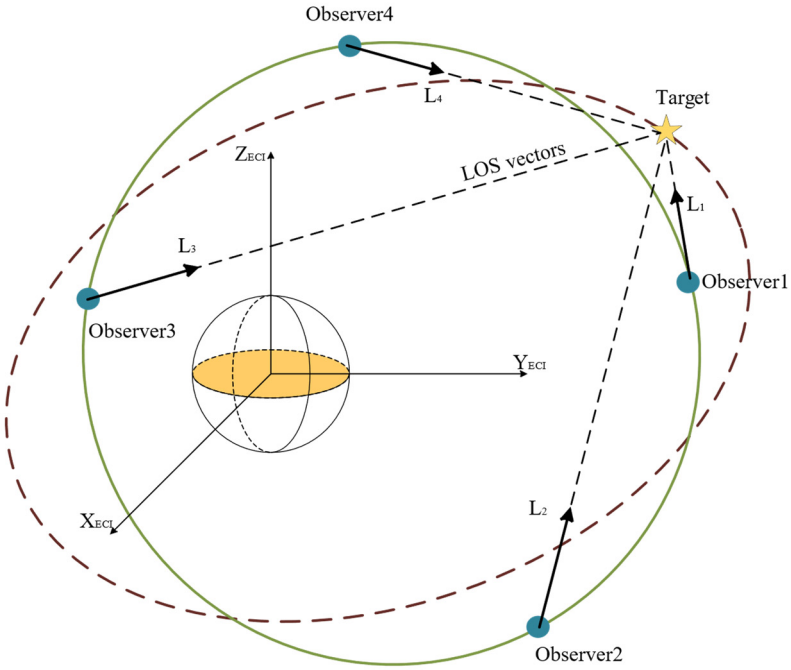


Figure 1. Observation scenario.

The orbital configuration parameters of the target satellite and observation satellites used in the simulation are listed in Table 1. From left to right, the columns correspond to the semi-major axis a, eccentricity e, inclination i, right ascension of the ascending node Ω, argument of perigee ω, and true anomaly ν.

Table 1. Orbital parameters of target and observer satellites.

Spacecraft	a (km)	e	i (deg)	Ω (deg)	ω (deg)	ν (deg)
Target	7978.137	0.12	53.0	40.0	30.0	10.0
Observer 1	8114.137	0.14	56.0	25.0	45.0	75.0
Observer 2	8114.137	0.14	56.0	60.0	20.0	145.0
Observer 3	8278.137	0.16	52.0	85.0	70.0	220.0
Observer 4	8278.137	0.16	52.0	15.0	110.0	300.0

To evaluate the orbit determination performance of the proposed method under space-based multi-satellite cooperative observation conditions, the Extended Kalman Filter (EKF), Unscented Kalman Filter (UKF), and Cubature Kalman Filter (CKF) are selected as comparative algorithms, and their performance is comprehensively analyzed in terms of orbit determination accuracy and computational efficiency.

Three numerical experiments are performed. In the first scenario, both measurement noise and process noise are conventional Gaussian noise. The second scenario assumes non-Gaussian measurement noise with a small number of outlier noises added. The third scenario increases the number of outliers in the measurement noise, and the process noise information is unknown ($Q_{ture} = 4 \times Q$). The numerical simulations were implemented in Python 3.10. The target orbit was propagated using a numerical integration method under the J2 perturbation model, while the remaining unmodeled perturbations were represented by process noise. The measurement data were generated at a sampling interval of 0.5 s, and the total simulation duration was 1500 s. Four observer satellites were used to continuously observe one target spacecraft. The same initial orbital configuration and WLS-derived initial state were used for all compared filters to ensure fairness.

The Root Mean Square Error (RMSE) is used to measure the overall accuracy of the filter.

$$RMSE = \sqrt{\frac{1}{n}\sum_{i=1}^{n}|\hat{r}_i - r_i|^2} \tag{49}$$

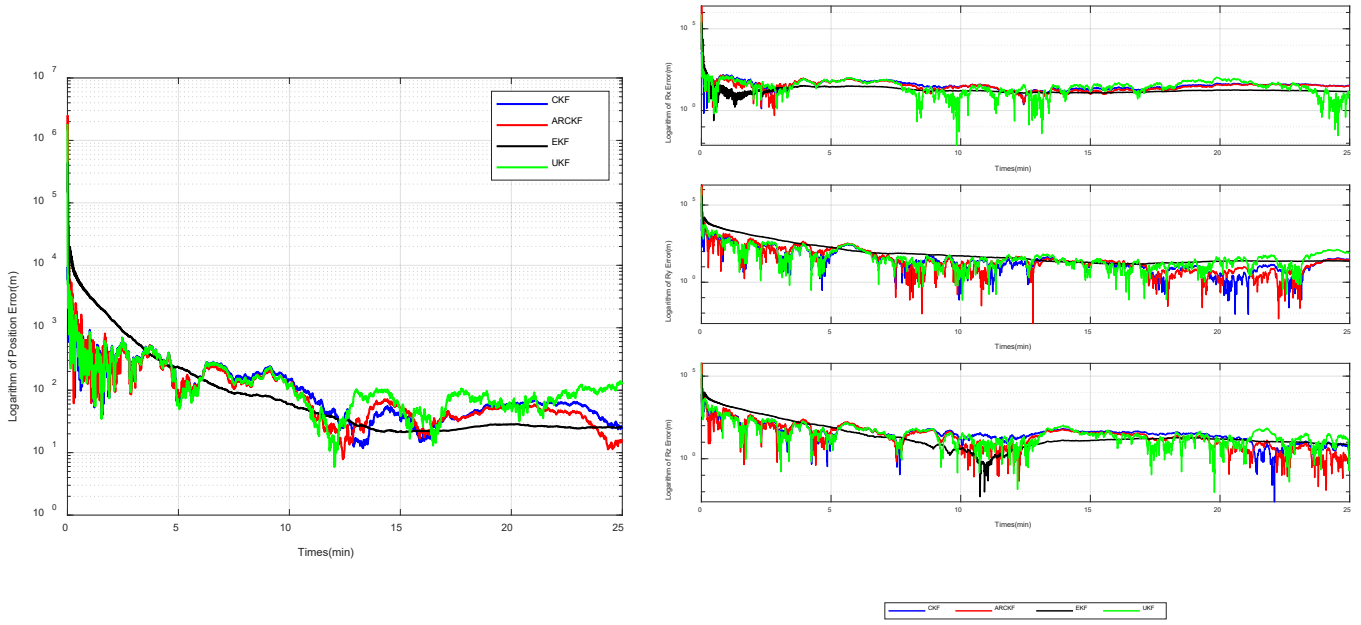
where $\hat{r}$ is the estimated target position, and r_i is the numerically generated true target position. In all simulation scenarios, the initial state covariance matrix is set as $P_0 = diag(10^8, 10^8, 10^8, 10^4, 10^4, 10^4)$, where the first three diagonal elements correspond to the position variances with units of m^2, and the last three elements correspond to the velocity variances with units of $(m/s)^2$.

4.1. Scenario 1

In this scenario, it is assumed that both the measurement noise and the process noise are Gaussian noise. The angular measurement noise is modeled as zero-mean Gaussian noise, i.e., θ, φ sim $N(0, \sigma^2)$, where σ is given in arcseconds.

The measurement noise is $\theta/\varphi \sim N(0, 1.5^2)$.

The process noise is $q = 1 \times 10^{-8}$ m^2/s^3. Figure 2 present the simulation results for Scenario 1.



(**a**) Logarithm of position error for Scenario 1

(**b**) Logarithm of three−axis error for Scenario 1

Figure 2. Logarithm of position error for Scenario 1.

Under Gaussian noise conditions, all algorithms demonstrate stable convergence with no significant disparity in orbit determination accuracy. However, the ARCKF exhibits a longer computation time. As indicated by the algorithm runtime data provided in Table 2, the ARCKF algorithm requires more time to execute. Therefore, reducing the computational complexity of the algorithm remains a key direction for future research.

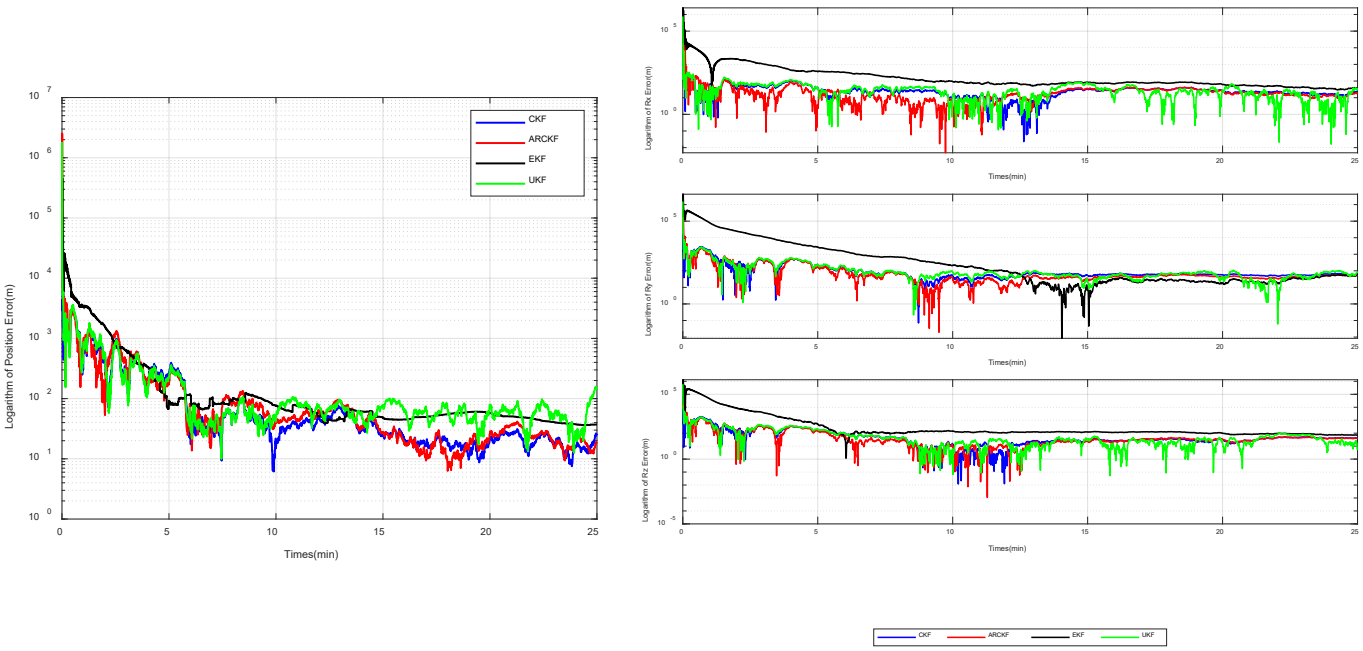
Table 2. RMSE of the position error in Scenario 1.

Algorithm	R_x (m)	R_y (m)	R_z (m)	RMSE (m)	Time (s)
EKF	6.8	6.9	6.4	6.7	3.83
UKF	5.6	5.1	6.0	5.6	6.75
CKF	4.3	3.9	4.7	4.3	6.47
ARCKF	4.2	3.6	4.3	4.1	7.15

4.2. Scenario 2

In this scenario, a small number of strong outliers are added to the measurement noise. Its angular unit is also arcseconds.

The measurement noise is $\theta/\varphi \sim 0.99N(0, 1.5^2) + 0.01N(0, 20^2)$. Figure 3 present the simulation results for Scenario 2.



(**a**) Logarithm of position error for Scenario 2 (**b**) Logarithm of three−axis error for Scenario 2

Figure 3. Logarithm of position error for Scenario 2.

In the presence of a limited number of measurement outliers, the filtering accuracy of EKF, UKF, and CKF is affected due to their sensitivity to non-Gaussian noise. In contrast, ARCKF incorporates the Maximum Correntropy Criterion to suppress the influence of abnormal measurements through the hybrid-kernel robust weighting strategy. As shown in Table 3, ARCKF reduces the position RMSE by 60.5%, 41.9%, and 30.5% compared with EKF, UKF, and CKF, respectively. These results indicate that ARCKF can improve filtering accuracy and demonstrate a slight advantage in orbit estimation performance under this scenario.

Table 3. RMSE of the position error in Scenario 2.

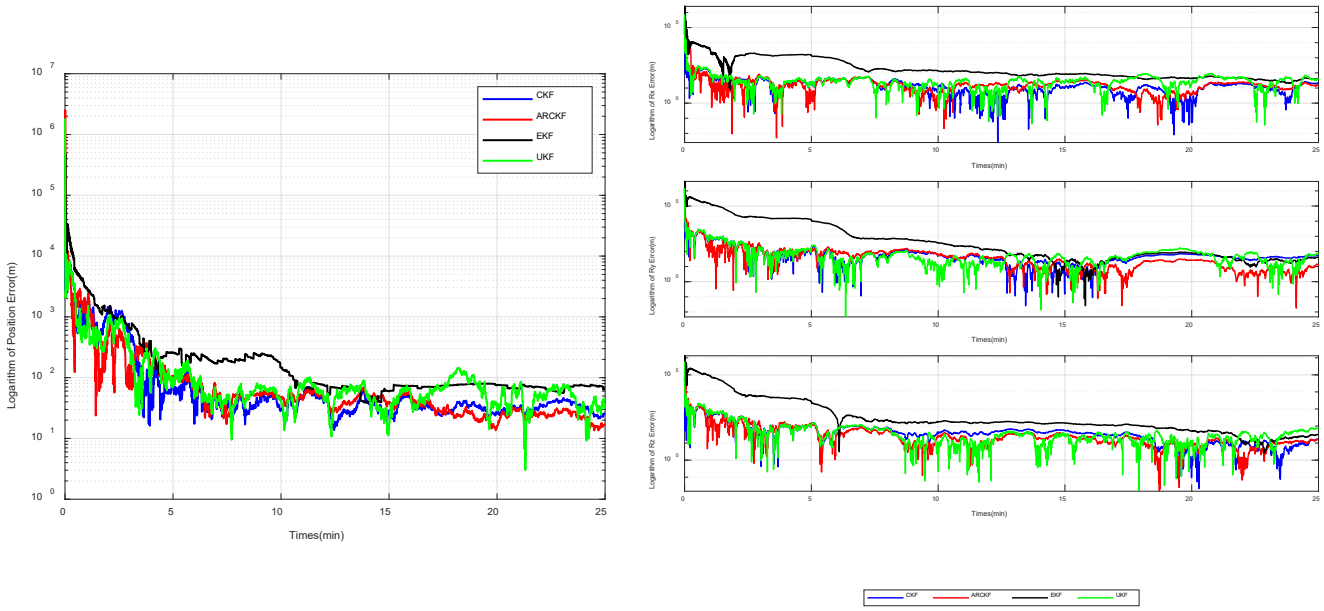
Algorithm	R_x (m)	R_y (m)	R_z (m)	RMSE (m)	Time (s)
EKF	42.6	38.1	41.9	41.0	3.86
UKF	28.4	26.9	28.5	27.9	6.87
CKF	21.5	24.5	23.8	23.3	6.48
ARCKF	16.2	14.9	17.5	16.2	7.22

4.3. Scenario 3

In this scenario, the measurement noise is non-Gaussian, where:

The measurement noise is $\theta/\varphi \sim 0.97N(0, 1.5^2) + 0.03N(0, 25^2)$, and its angular unit is arcseconds.

The process noise is increased to $Q_{ture} = 10 \times Q$. Figure 4 present the simulation results when the process noise statistical information is insufficient and the system noise follows a non-Gaussian distribution.



(**a**) Logarithm of position error for Scenario 3 (**b**) Logarithm of three−axis error for Scenario 3

Figure 4. Logarithm of position error for Scenario 3.

In the presence of measurement outliers and unknown process noise, the filtering performance of EKF, UKF, and CKF degrades significantly, with brief divergence even occurring. In contrast, ARCKF incorporates the Maximum Correntropy Criterion to suppress the influence of outliers and adaptively compensates for process noise modeling errors through online adjustment of the process noise intensity. As shown in Table 4, ARCKF reduces the position RMSE by 82.3%, 76.3%, and 70.0% compared with EKF, UKF, and CKF, respectively.

Table 4. RMSE of the position error in Scenario 3.

Algorithm	R_x (m)	R_y (m)	R_z (m)	RMSE (m)	Time (s)
EKF	165.4	148.2	172.6	162.5	3.91
UKF	121.7	109.3	133.4	121.6	6.91
CKF	96.8	88.5	102.1	96.0	6.52
ARCKF	28.9	25.4	31.6	28.8	7.35

To further evaluate the statistical robustness of the proposed method under the combined influence of non-Gaussian measurement noise and unknown process noise, 50 independent Monte Carlo simulations were performed based on Scenario 3. For each simulation run, the measurement noise, outlier sequence, and process noise disturbance were regenerated independently. The EKF, UKF, CKF, and ARCKF were then applied separately for state estimation. The position RMSE variations of the four algorithms over the 50 Monte Carlo runs are presented in Figure 5, and the corresponding statistical results are summarized in Table 5.

Table 5. Statistical results of the position RMSE over 50 Monte Carlo simulations.

Algorithm	Min (m)	Max (m)	Mean (m)
EKF	70.8	231.3	168.2
UKF	73.7	176.8	123.4
CKF	50.7	129.2	95.3
ARCKF	21.3	41.2	30.8

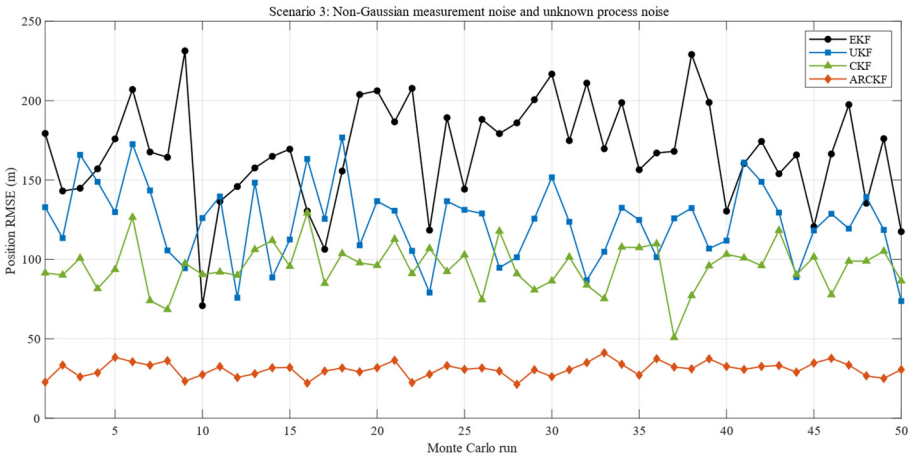


Figure 5. Position RMSE statistics over 50 Monte Carlo simulations.

As shown in Figure 5, the estimation errors of the EKF, UKF, and CKF exhibit different degrees of fluctuation under multiple random noise realizations. The EKF is the most sensitive to the combined effects of non-Gaussian measurement noise and unknown process noise. Over the 50 Monte Carlo simulations, its average position RMSE reaches 168.2 m, with a maximum value of 231.3 m. Compared with the EKF, the UKF and CKF provide improved estimation accuracy, but they still show relatively large error fluctuations in the presence of abnormal measurements and process noise uncertainty. Their average position RMSE values are 123.4 m and 95.3 m, respectively. By contrast, the ARCKF consistently maintains a lower position RMSE over the 50 simulations. The minimum, maximum, and average position RMSE values of the ARCKF are 21.3 m, 41.2 m, and 30.8 m, respectively. Although different noise realizations lead to slight fluctuations in the ARCKF results, its error range is much narrower than those of the other three algorithms, indicating superior statistical robustness. In terms of the average position RMSE, the ARCKF achieves reductions of approximately 81.7%, 75.0%, and 67.7% compared with the EKF, UKF, and CKF, respectively. These results indicate that ARCKF maintains stable and high-precision orbit estimation performance in complex noise environments.

5. Conclusions

This paper proposes an orbit determination method that integrates a plane-constrained observation model with adaptive robust filtering (ARCKF), providing a solution for high-precision orbit determination in complex noise environments. A multi-satellite plane-constrained observation model is constructed to convert angular measurements into geometric constraints, and the weighted least squares method is employed to rapidly solve for the initial position and velocity. A hybrid kernel maximum correntropy criterion is designed, and a covariance matching-based adaptive factor is proposed to adjust the process noise intensity online, thereby enhancing the algorithm's robustness. In conditions of unknown sensor noise statistics and uncertain dynamic disturbances, ARCKF reduces the position RMSE to 30.8 m, corresponding to reductions of 81.7%, 75%, and 67.7% relative to EKF, UKF, and CKF, respectively, although its computation time increases to 7.35 s. The results demonstrate that under angles-only measurement constraints with non-Gaussian noise and unknown process noise, the algorithm maintains high accuracy and fast convergence characteristics, effectively reducing orbit estimation errors. Furthermore, considering the requirements of real-time performance and limited computational resources in onboard applications, future work should focus on lightweight algorithm design from an engineering implementation perspective. Specifically, the cubature point propagation process can be parallelized to reduce the computational time required in the state prediction stage. In

addition, an adaptive triggering strategy can be adopted so that robust weight updating is performed only when abnormal residuals or decreased filtering consistency is detected, thereby avoiding complex weight correction at every filtering step. These measures can reduce the computational burden while maintaining the robustness and estimation accuracy of the algorithm, further improving its engineering applicability in practical onboard orbit determination missions. Future research will further investigate these two optimization directions in depth.

Author Contributions: Conceptualization, M.L.; methodology, M.L. and M.H.; software, M.L. and Y.M.; validation, T.W.; formal analysis, T.W.; investigation, N.Q.; resources, N.Q.; data curation, X.Z.; writing—original draft preparation, M.L., T.W. and X.Z.; writing—review and editing, M.H., N.Q. and Y.M.; visualization, X.Z. and Y.M.; supervision, M.H. and N.Q.; project administration, X.Z.; funding acquisition, M.H. All authors have read and agreed to the published version of the manuscript.

Funding: This work was supported in part by the National Natural Science Foundation of China (grant number 12272104), and in part by the National Natural Science Foundation of China (grant number U22B2013).

Data Availability Statement: The data used to support the findings of this study are included within the article.

Conflicts of Interest: The authors declare that they have no known competing financial interests or personal relationships that could have appeared to influence the work reported in this paper.

References

1. Gu, Y.; Li, Z.; Liu, H.; Luo, Q.; Liu, H.; Wu, G. Multi-objective early warning mission planning by multiple satellites using a critical task aggregation-based NSGA-II algorithm. *Adv. Space Res.* **2026**, *77*, 11199–11219. [CrossRef]
2. Lee, D.; Hwang, S.S. Enhanced Real-Time Onboard Orbit Determination of LEO Satellites Using GPS Navigation Solutions with Signal Transit Time Correction. *Aerospace* **2025**, *12*, 508. [CrossRef]
3. Cao, J.; Liu, L.; Liu, Y.; Su, W.; Hu, S. A Simulation Study of Orbit Determination for Lunar Probe via Relay Satellite. In *Proceedings of the 28th Conference of Spacecraft TT&C Technology in China: Openness, Integration and Intelligent Interconnection, Beijing, China, 8–10 November 2016*; Springer: Singapore, 2018; pp. 143–151.
4. Aghav, S.T.; Gangal, S.A. Simplified orbit determination algorithm for low earth orbit satellites using spaceborn GPS navigation sensor. *Artif. Satell.* **2014**, *49*, 81–99. [CrossRef]
5. Amishima, T. Theoretical Error Analysis of GEO Orbit Determination by TDOA of Multiple Ground Stations and its Applications to Geolocation. *IEICE Trans. Commun.* **2025**, *E108-B*, 1263–1271. [CrossRef]
6. Qu, W.; Huang, Y.; Xu, J.; Sun, S.; Zhou, S.; Yang, Y.; He, B.; Hu, X. Precise Orbit Determination Using Satellite Laser Ranging and Inter-satellite Link Observations for BDS-3 Satellites. *Acta Geod. Cartogr. Sin.* **2024**, *52*, 1437.
7. Li, X.; Li, Y.; Zhang, K.; Fu, Y.; Zhang, W.; Zheng, H. Precise Orbit Determination for LEO Constellation Based on Onboard GNSS Observations, Inter-satellite Links and Ground Tracking Data. *GPS Solut.* **2025**, *29*, 107. [CrossRef]
8. Shimane, Y.; Tomita, K.; Ho, K. Cislunar Space Situational Awareness Constellation Design and Planning with Facility Location Problem. *J. Spacecr. Rocket.* **2025**, *62*, 1938–1960. [CrossRef]
9. Ma, Y.; Li, M.; Wang, T.; Ke, W.; Yang, N.; Huo, M. Design of the Perception Simulation System for Distributed Satellite Constellations. In *Proceedings of the 2nd Aerospace Frontiers Conference, Beijing, China, 11–14 April 2025*; Springer: Singapore, 2025; Volume 4, pp. 185–204.
10. Gauss, C.F. *Theoria Motus Corporum Coelestium in Sectionibus Conicis Solem Ambientium*; F. Perthes and I.H. Besser: Hamburg, Germany, 1809.
11. Laplace, P.S. Mémoire sur la Détermination des Orbites des Comètes. In *Œuvres complètes de Laplace*; Gauthier-Villars et fils: Paris, France, 1894; Volume 10, pp. 93–146.
12. Gibbs, J. On the determination of elliptic orbits from three complete observations. *Mem. Natl. Acad. Sci.* **1889**, *4*, 79–104.
13. Bate, R.R.; Mueller, D.D.; White, J.E. *Fundamentals of Astrodynamics*; Dover Publications: New York, NY, USA, 1971.
14. Mancini, M.; Christian, J.A. Solving the Gibbs problem with algebraic projective geometry. *J. Spacecr. Rocket.* **2025**, *62*, 251–256. [CrossRef]
15. Mancini, M.; Duff, T.; Leykin, A.; Christian, J.A. Geometric solution to the angles-only initial orbit determination problem. *J. Astronaut. Sci.* **2025**, *72*, 49. [CrossRef]

16. Guan, Y.; He, Y.; Nie, T.; Zhu, S. A Fast Space-Based Angles-Only Initial Orbit Determination Algorithm for Very Short Arcs. In Proceedings of the 2025 44th Chinese Control Conference (CCC), Chongqing, China, 28–30 July 2025.
17. Kruger, J.; D'Amico, S. Autonomous Angles-Only multitarget tracking for spacecraft swarms. *Acta Astronaut.* **2021**, *189*, 514–529. [CrossRef]
18. Pu, J.; Li, S.; Liu, J.; Guo, P.; Wang, W. Space-Based Orbit Determination and Time Synchronization Method for Three Typical Cislunar Orbits. *J. Deep Space Explor.* **2023**, *10*, 641–651.
19. Kinatas, H.; Hajiyev, C. Preliminary Orbit Estimation for Turksat 5B via Extended and Unscented Kalman Filtering. In *Proceedings of the 2nd International Conference on Information Technologies and Their Applications, Baku, Azerbaijan, 23–25 April 2024*; Springer Nature: Cham, Switzerland, 2024.
20. Ren, X.; Yang, Y.; Zhu, J.; Xu, T. Comparing Satellite Orbit Determination by Batch Processing and Extended Kalman Filtering Using Inter-satellite Link Measurements of the Next-generation BeiDou Satellites. *GPS Solut.* **2019**, *23*, 25. [CrossRef]
21. Bierman, G.J. *Factorization Methods for Discrete Sequential Estimation*; Courier Corporation: San Francisco, CA, USA, 2006.
22. Lou, Y.; Dai, X.; Gong, X.; Li, C.; Qing, Y.; Liu, Y.; Peng, Y.; Gu, S. A review of real-time multi-GNSS precise orbit determination based on the filter method. *Satell. Navig.* **2022**, *3*, 15. [CrossRef]
23. Hippelheuser, J.; Elgohary, T.A. Inertial space-based orbit estimation: A new measurement model for multiple observers. *Acta Astronaut.* **2021**, *181*, 717–732. [CrossRef]
24. Fossà, A.; Armellin, R.; Delande, E.; Losacco, M.; Sanfedino, F. A multifidelity approach to robust orbit determination. *Acta Astronaut.* **2024**, *214*, 277–292. [CrossRef]
25. Xu, Y.; Feng, X.; Li, S.; Pu, J.; Chen, S.; Wang, W. Research on Sliding-Window Batch Processing Orbit Determination Algorithm for Satellite-to-Satellite Tracking. *Aerospace* **2025**, *12*, 662. [CrossRef]
26. Wang, J.; Lyu, D.; He, Z.; Zhou, H.; Wang, D. Cauchy kernel-based maximum correntropy Kalman filter. *Int. J. Syst. Sci.* **2020**, *51*, 3523–3538. [CrossRef]
27. Chu, S.; Qian, H.; Yan, S.; Ding, P. Adaptive robust maximum correntropy cubature Kalman filter for spacecraft attitude estimation. *Adv. Space Res.* **2023**, *72*, 3376–3385. [CrossRef]

Disclaimer/Publisher's Note: The statements, opinions and data contained in all publications are solely those of the individual author(s) and contributor(s) and not of MDPI and/or the editor(s). MDPI and/or the editor(s) disclaim responsibility for any injury to people or property resulting from any ideas, methods, instructions or products referred to in the content.